RAA 2019 Vol. **19** No. **11**, 163(10pp) doi: 10.1088/1674–4527/19/11/163
© 2019 National Astronomical Observatories, CAS and IOP Publishing Ltd.
http://www.raa-journal.org *http://iopscience.iop.org/raa*

Research in Astronomy and Astrophysics

Simulations and software development for the Hard X-ray Imager onboard ASO-S

Yang Su[1,2], Wei Liu[1], You-Ping Li[1,2], Zhe Zhang[1], Gordon J. Hurford[3,4], Wei Chen[1,2], Yu Huang[1,2], Zhen-Tong Li[1,2], Xian-Kai Jiang[1,2], Hao-Xiang Wang[1,2], Fan-Xiao-Yu Xia[1,2], Chang-Xue Chen[1,5], Wen-Hui Yu[1,2], Fu Yu[1,2], Jian Wu[1] and Wei-Qun Gan[1,2]

[1] Key Laboratory of Dark Matter and Space Astronomy, Purple Mountain Observatory, Chinese Academy of Sciences, Nanjing 210034, China; *yang.su@pmo.ac.cn*
[2] School of Astronomy and Space Science, University of Science and Technology of China, Hefei 230026, China
[3] University of Applied Sciences and Arts Northwestern Switzerland, Bahnhofstrasse 6, 5210 Windisch, Switzerland
[4] Space Science Laboratory, University of California, 7 Gauss Way, 94720 Berkeley, USA
[5] School of Space Science and Physics, Shandong University, Weihai 264209, China

Received 2019 July 2; accepted 2019 September 6

Abstract China's first solar mission, the Advanced Space-based Solar Observatory (ASO-S), is now changing from Phase B to Phase C. Its main scientific objectives are summarized as '1M2B', namely magnetic field and two types of bursts (solar flares and coronal mass ejections). Among the three scientific payloads, Hard X-ray Imager (HXI) observes images and spectra of X-ray bursts in solar flares. In this paper, we briefly report on the progresses made by the HXI science team (data and software team) during the design phase (till May 2019). These include simulations of HXI imaging, optimization of HXI grids, development of imaging algorithms, estimation of orbital background, as well as in-orbit calibration plan. These efforts provided guidance for the engineering, improved HXI's imaging capability and reduced the cost of the instrument.

Key words: techniques: X-ray imaging — techniques: simulation — Sun: X-rays — Sun: flares

1 INTRODUCTION

The Advanced Space-based Solar Observatory (ASO-S) is China's first solar mission (Gan et al. 2019), dedicated to three major scientific objectives, photospheric magnetic field, solar flares and corona mass ejections (CMEs). One of the three payloads onboard ASO-S, the Hard X-ray Imager (HXI, Zhang et al. 2019), will observe images and spectra of flare X-ray bursts in the energy range from ∼30 to 200 keV (the recorded energies are in the range from ∼10 to 400 keV). HXI can also provide reconstructed images for analysis of imaging spectroscopy.

Solar eruptive events (SEEs) are the most intense energy release in the solar system (see the reviews on flares in Priest & Forbes 2002; Fletcher et al. 2011; Shibata & Magara 2011; Benz 2017). By releasing previously stored magnetic energy through magnetic reconnection and other processes, they cause enhanced emission across the entire electromagnetic spectrum from radio to X-rays, Gamma-rays, a large number of accelerated particles and rapid ejection of large-scale magnetic flux ropes. These are the main factors of potentially disastrous space weather.

Flare X-ray bursts usually come from two types of sources. Soft X-rays are mostly thermal bremsstrahlung emission from heated plasma at temperatures from a few million K to tens of MK. Hard X-rays are mostly non-thermal bremsstrahlung emission from accelerated electrons. They are the direct products of the reconnection process and energy release in flares, and therefore have been one focus of solar observations ever since the space era began (for reviews see Holman et al. 2011; Raymond et al. 2012). Energetic electrons are also responsible for the impulsive enhancement in emissions at other wavelengths and spectral lines, such as white light, radio, ultraviolet (UV), extreme ultraviolet (EUV), Hα line, Lymanα line, etc.

Therefore, X-ray images are widely applied in studies of flares, especially in the diagnosis of plasma heat-

ing, particle acceleration, reconnection, first energy release site, spectral line diagnosis, etc. Full-disk X-ray spectra and imaging spectra can be utilized to derive the physical parameters of thermal plasma and accelerated particles. They tell us the amount of energy contained therein and help us understand the whole process of flares. The imaging spectra of an individual source, in particular, contain important information on the acceleration, transportation, thermalization and emission of energetic electrons.

More importantly, HXI and STIX onboard the Solar Orbiter will, for the first time, image the Sun in X-rays simultaneously from two different viewing angles (see Krucker et al. 2019, for more details). Such imagery will provide us with long-awaited observations, which are crucial for understanding the anisotropic nature of the distribution and emission of energetic electrons (Brown 1972; Casadei et al. 2017). After careful cross calibration, the images and spectra obtained by HXI and STIX will be studied with joint analysis software.

HXI implements a Fourier transform imaging technique with 91 subcollimators to modulate the X-rays. Unlike the high energy solar mission RHESSI (Lin et al. 2002), HXI cannot spin to cover all position angles due to the requirements of other payloads. Instead, it behaves like Yohkoh/HXT (Kosugi et al. 1991) and STIX. It measures 45 visibilities from 44 pairs of cos-sin subcollimators, plus one single set of three subcollimators (see Fig. 1), which cover ten different pitches (spatial frequency) and five position angles (at most) for each subcollimator. An improvement has been made compared with previous instruments by including total flux monitors and background monitors, which have the same type of detectors used for imaging. They can significantly improve the accuracy in the calculations of visibilities and the quality of reconstructed images.

In order to cover a wide range of spatial scales of various X-ray sources, the desired spatial resolution corresponding to the subcollimators ranges from $\sim$3 (full width at half maximum, FWHM) to at least 100 arcsec. Therefore, we now use a total of 10 groups of grids with pitches having sizes 36, 52, 76, 108, 156, 224, 344, 524, 800 and 1224 μm to cover this range. The front and rear grids are separated by a distance of nearly 1200 mm (Zhang et al. 2019). Statistical studies using RHESSI data have shown that most HXR sources have sizes between $\leq$2 and $\sim$20 arcsec (Dennis & Pernak 2009; Warmuth & Mann 2013). Therefore, we optimized the selection of pitches to ensure that six fine pitches out of ten are used to enhance the UV sampling for the corresponding spatial range.

HXI records a count spectrum from the LaBr3 detector behind each subcollimator in two observation modes. One is normal mode with cadence of 4 s, and the other one is burst mode with fast cadence pre-selected from one of the four settings, 0.125, 0.25, 0.5 or 1 s. Images of the X-ray source in different energy bands can then be reconstructed by selected imaging algorithms in HXI software.

2 MAIN TASKS OF HXI SCIENCE TEAM

The HXI data and software team is responsible for a number of important tasks that are essential for achieving HXI's scientific objectives. These include, but are not limited to,

(1) HXI imaging simulation.
(2) Simulation of in-orbit background and detector response.
(3) Development of imaging algorithms.
(4) Optimization of HXI design (mainly on grids and subcollimators).
(5) Definition of science data products.
(6) Production, calibration and release of science data.
(7) Development of HXI analysis software.
(8) In-orbit self-calibration for HXI grid subcollimators.
(9) Corrections of images and spectra for instrumental effects.
(10) Release and updates of all related documents.

3 IMAGING ALGORITHMS

Imaging algorithms are the key to reconstructing images of X-ray sources from modulated fluxes. In general, there are two types of imaging algorithms. One is pattern-based, and the other is visibility-based. The HXI science team has investigated 15 algorithms, most of which are being used in the RHESSI software (more details can be found at *https://hesperia.gsfc.nasa.gov/rhessi3/software/imaging-software/image-algorithm-summary/index.html*). Six of them were selected as the most basic components of HXI imaging software. These are Back projection, Clean, Forward Fit, VIS_BP, VIS_Clean and VIS_Forward Fit. More imaging methods (such as Pixon, MEM_GE) will be developed by the HXI science team and the community, and provided in the HXI software package after the launch of ASO-S. It should be pointed out that almost all current visibility-based methods can be used without further modifications, once the HXI visibilities are calculated and corrected for instrumental effects.

3.1 Back Projection

Back projection (Mertz et al. 1986) is the "most straightforward and basic method of image reconstruction" (Hurford

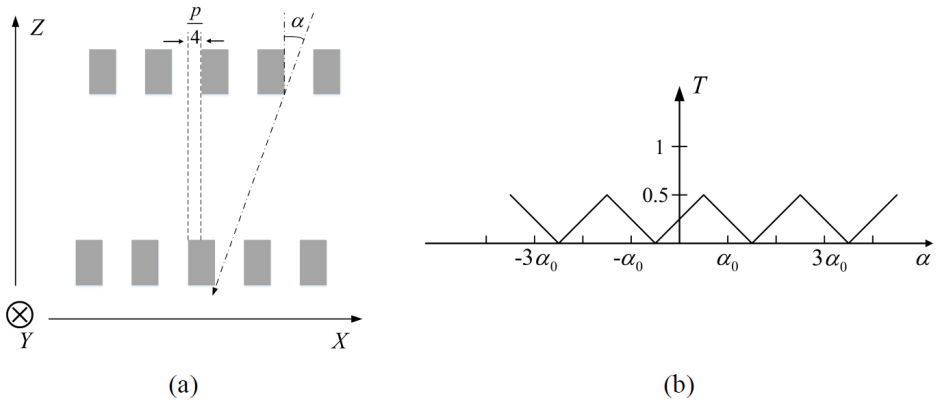

Fig. 1 (a) This panel displays an example of sin-type subcollimator with front and rear grids that are shifted by 90 degrees in phase (pitch/4). (b) This panel presents the corresponding triangular response function (in ideal case). α is the incidence angle, and T is the transmission rate or grid response (ratio of flux received by the detector to total flux).

et al. 2002). The method makes use of grid response (or pattern, the two-dimensional (2D) extension of the triangular response function along slits, see Fig. 2) or visibilities to obtain a dirty map. When using visibilities, it is basically a 2D inverse Fourier transform (Kilner & Nakano 1989). Since the corresponding procedure (VIS_BP) has been developed and implemented in Solar Software (SSW), here we focus on the pattern-based method.

For a single pixel m in detector i, its intensity can be written as,

$$I_m = \sum C_i \hat{P}_{i,m} = \sum C_i \frac{P_{i,m} - P_{m(\mathrm{avg})}}{\langle (P_{i,m} - P_{m(\mathrm{avg})})^2 \rangle}. \quad (1)$$

Here the expression is slightly different from that for rotating modulators (such as RHESSI, Hurford et al. 2002; Durouchoux et al. 1983). The i here means the i-th detector instead of the i-th time bin for RHESSI. C_i is the count rates ($\mathrm{cm}^{-2}\,\mathrm{s}^{-1}$) obtained from the i-th detector, $P_{i,m}$ is the pattern value at the pixel for the i-th detector, $P_{m(\mathrm{avg})}$ is the average pattern value for all the detectors and $\langle (P_{i,m} - P_{m(\mathrm{avg})})^2 \rangle$ is the corresponding variance.

3.2 Clean

The Clean method was originally developed for radio astronomy and is now widely employed in X-ray image reconstruction. It is basically a process of 'de-convolution' of the back projected image using the point spread function (PSFs). The HXI Clean method follows the same principle as RHESSI Clean presented in Hurford et al. (2002).

3.3 Forward Fit

The Forward Fit method assumes that the image/source has a certain shape, such as a circle, loop (curved elliptical Gaussian), etc., and fits the observation to find the best parameters for the sources. Therefore, it is often used to measure the size and other parameters of the source geometry (Aschwanden et al. 1999; Dennis & Pernak 2009). At this stage, the corresponding code for HXI is under development.

4 HXI SIMULATION

HXI simulation is one of the most important tasks during this stage. We implement two different simulations, HXI grid simulation and Geant 4 (GEometry ANd Tracking, Allison et al. 2006) physical simulation. The former is applied for fast simulation of HXI imaging performance, testing of imaging algorithms and improvements of HXI grid design. The latter is utilized for background simulation, detector response and verification of grid simulation results.

4.1 Determination of Grid Parameters

The initial grid configuration covers spatial resolutions from 3 to about 70 arcsec. After discussion and careful consideration, we now enlarged the coverage of spatial resolution to about 100 arcsec, allowing HXI to effectively modulate the X-rays from large sources. The UV sampling is changed to STIX type, which follows spirals instead of straight lines. This configuration has been commonly implemented in radio astronomy. Figure 3 presents a comparison of the UV sampling for RHESSI, STIX and HXI (initial and current configuration).

4.2 HXI Imaging Simulation

We simulated the geometry of HXI grids and subcollimators, and then calculated the transmission through the

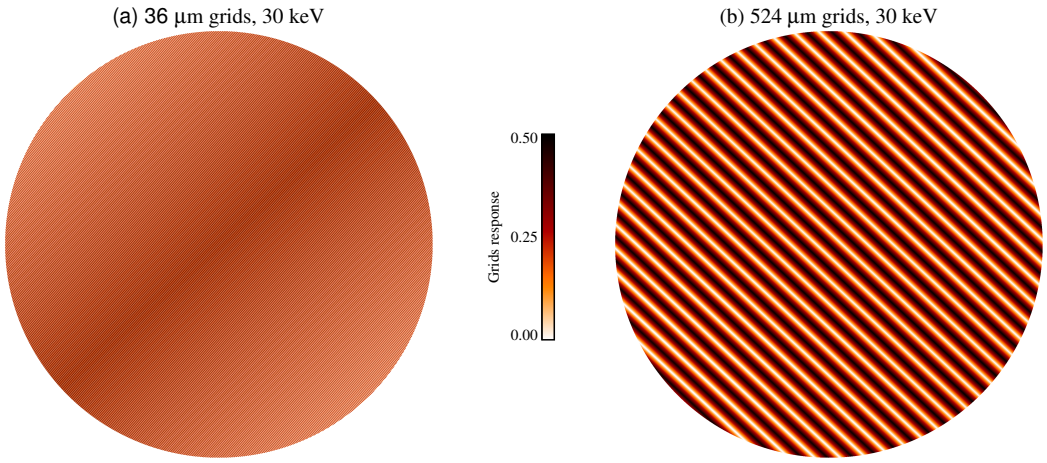

Fig. 2 Pattern images (grid response) for subcollimator with a pair of grids that have pitch of 36 (a) and 524 (b) μm. The responses are calculated for photons at 30 keV. The decreased responses in (a) at locations close to the edge of the field of view (FOV) are due to the effect of internal shadowing of the grids.

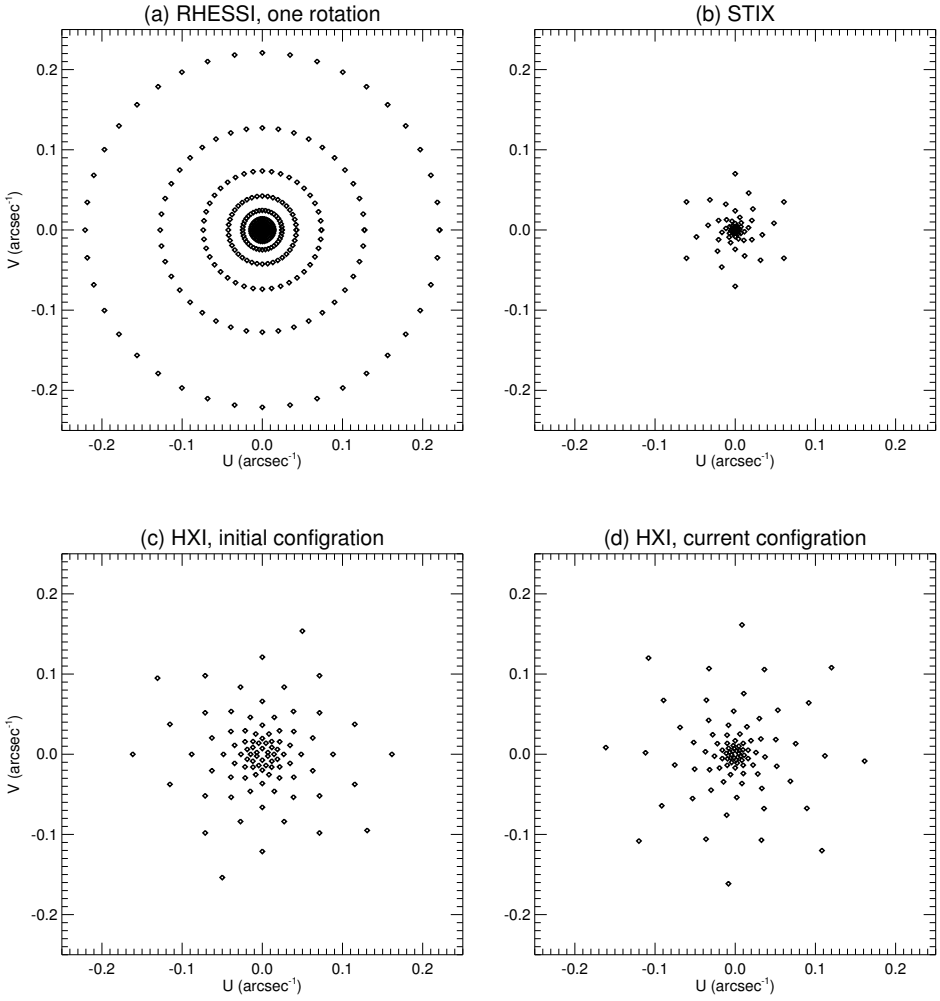

Fig. 3 UV sampling for RHESSI (a), STIX (b), HXI (c, initial configuration) and HXI (d, current configuration).

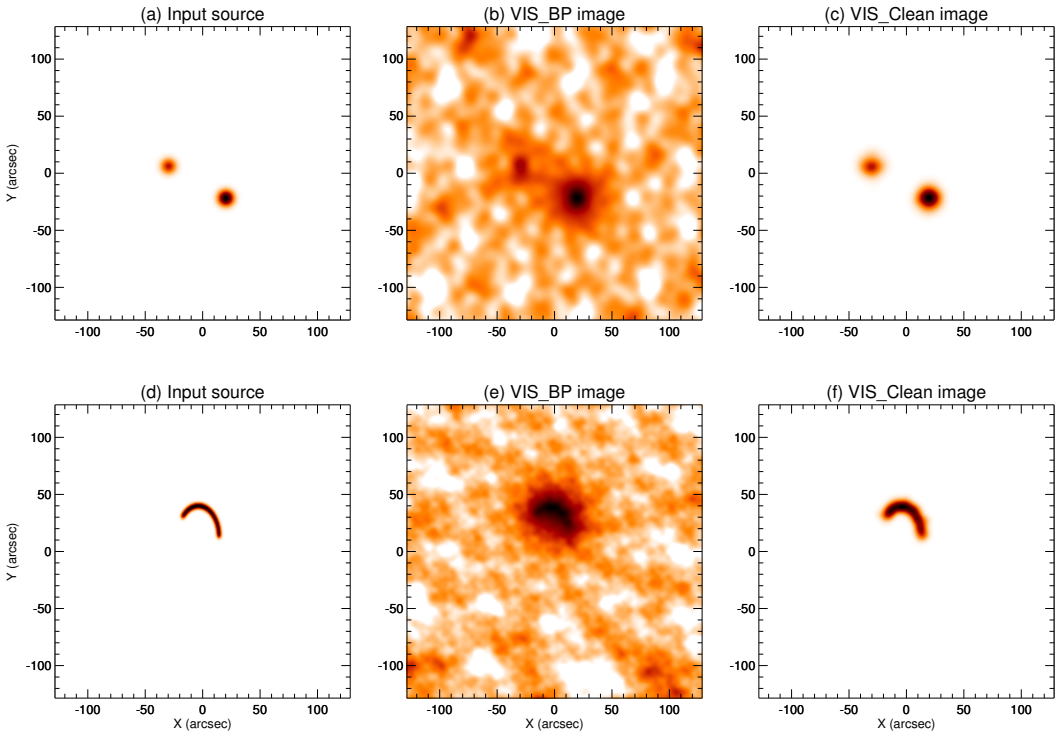

Fig. 4 Reconstructed HXI images for two simulated cases, one with two Gaussian footpoint sources (a) and the other a single loop (d). The two sources in (a) have the same size but a flux ratio of 2. The reconstructed images from VIS_BP and VIS_Clean are depicted in panels (b, c, e, f). The beam width was set to 4.5 and 3.6 arcsec in (c) and (f), respectively. Natural weighting was applied. The residual map is not added back in the final Clean image. Darker color means larger intensity here.

grids. As a result we obtain the response patterns for each grid pair. The results are also confirmed by the physical simulations in Geant 4. Together with the developed imaging algorithms, we are able to study the imaging capability of HXI.

Figure 4 displays the examples of two simulated X-ray images and the reconstructed images from two algorithms, VIS_BP and VIS_Clean. The two input images represent cases of two footpoint sources and a single loop source, respectively. Note that these reconstructions are under ideal conditions.

Figure 5 depicts the reconstructed images from five imaging algorithms for a more complex case, where three X-ray sources are included to represent footpoint sources and flare loops. The five methods include Back projection, Clean, vis_bp, vis_clean and MEM_GE.

4.3 Background Estimation and Detector Response

Knowledge of the background level in orbit is very important for most high energy imagers and spectrometers. It is also required for determining the radiation levels of the integrated radioactive sources needed for energy calibration. Accurate estimation of background is a very complex process. Here we only provide our preliminary results.

We mainly considered X-ray, Gamma-ray sources from CXB (diffuse Cosmic X-ray Background), Albedo, particles from HXI orbit, South Atlantic Anomaly (SAA) and radiation belt. Internal background from detectors and detector activation due to SAA passages is also included. The expected total background spectrum is depicted in Figure 6(a). This is calculated for the orbit outside SAA and radiation belt, but with stabilized background caused by detector activation considered. Currently, we use only the HXI mass model, but include an aluminum shell to simulate the effect of platform and other instruments. More accurate mass models of the satellite will be developed in the future. The details and results will be provided in a separate paper.

The detector response matrix is also obtained from simulations using Geant 4. Based on the response matrix (Fig. 6(b)), we calculated the expected count spectra for three flares in different GOES soft X-ray (SXR) classes. Their spectra were observed by RHESSI on 2011 Sep. 06 (X2), 2014 Sep. 23 (M2) and 2011 Dec. 25 (C7). The results are also exhibited in Figure 6(a). We conclude that HXI can image X-ray flares above M1 class, and may ob-

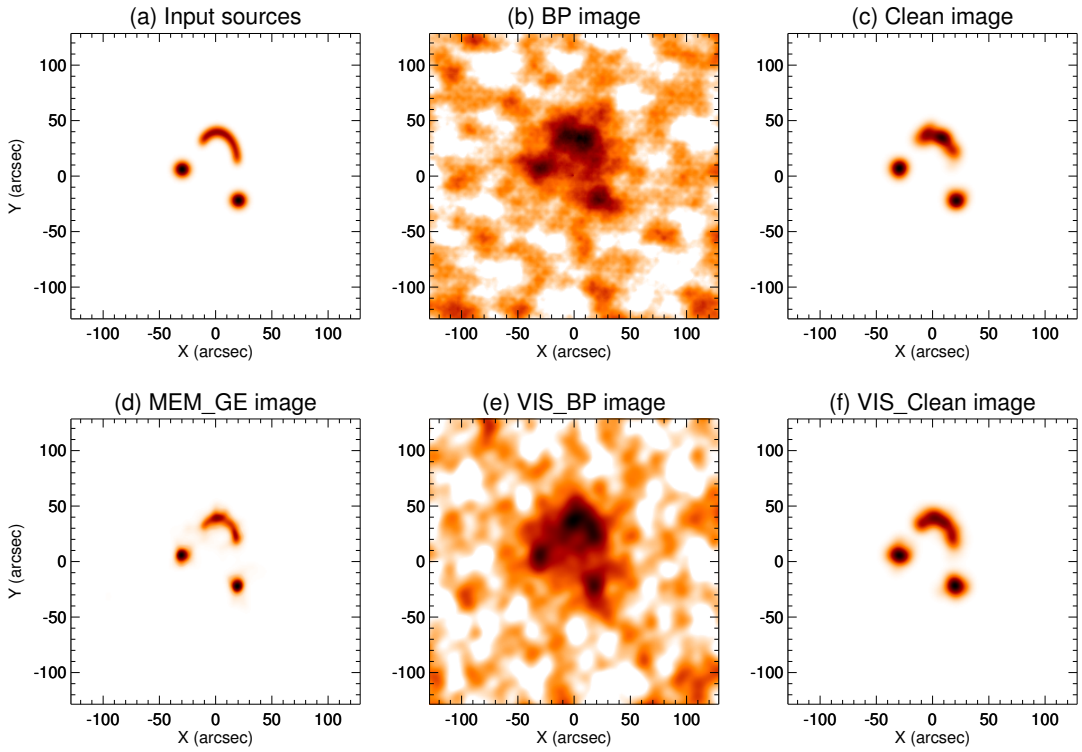

Fig. 5 Same as Fig. 4 but for a more complex case and five different imaging methods. The simulated flare X-ray image consists of two footpoint sources and a loop structure. Here the subcollimators with the finest grids (36 μm) are not used in MEM_GE, VIS_BP and VIS_Clean.

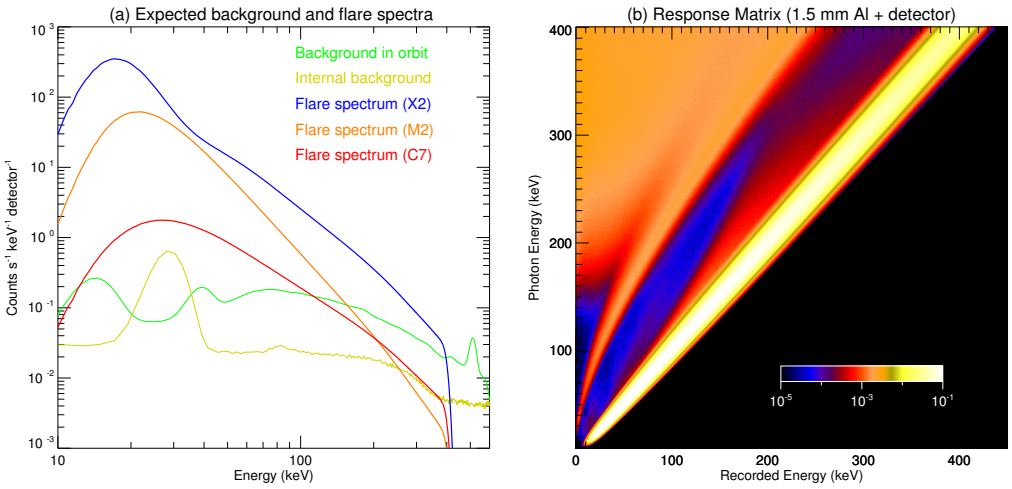

Fig. 6 (a) Estimated background for a single HXI detector (preliminary results) and expected count spectra for three flares at X2, M2 and C7 GOES class. The detector area used here is half of the rear grids. The rapid drop in fluxes close to 400 keV is caused by the limited range of the response matrix. (b) Detector response matrix (preliminary results) obtained from Geant 4 simulation. The simulation was done for a single detector with a layer of aluminum in front that has thickness of 1.5 mm.

serve some C-class flares if there are strong HXR emissions. Since the total flux monitor has larger effective area, we expect that HXI will obtain useful spectra from flares larger than C5-level. More complete and detailed mass models of ASO-S will be utilized in the future to improve the estimation of both orbital background and detector response matrix.

4.4 Grid Thickness

Many factors can make the subcollimators non-ideal. Here we first consider the effect of finite thickness of grids, as it is almost inevitable and has significant impact for fine grids, as well as image quality. Based on the simulation software and imaging algorithms, we are able to study and improve HXI imaging capabilities. What we mainly consider in determining grid parameters include: (1) scientific requirement on spatial resolution, (2) image quality, (3) cost, (4) manufacturing time and (5) technical limitations.

The effect of grid internal shading caused by the finite thickness of grids makes the triangular response functions non-ideal. The grid thickness (2 mm) determined at early stages satisfies the imaging requirement at both low energies at ∼30 keV and high energies at 200 keV. If the grid is too thin, high energy photons can easily penetrate the grids, resulting in less modulation of incoming light. These effects must be considered in the calculation of pattern and visibilities.

Our simulation and calculation showed that the fine grids blocked more incoming lights than those in the ideal case, and caused decrease of modulation efficiency. The effect is more significant for a source at larger distance away from the grid's central line (across the slit direction). The coarse grids are less affected due to their wide slits. In Figure 7, we display a comparison of the ideal triangular response functions and realistic ones for a pair of grids with pitch 36 μm.

We plotted the modulation efficiency as a function of grid thickness for two different energies, 30 and 200 keV, respectively. This demonstrated that with increasing thickness, the efficiency decreases fast at low energy but increases at high energy. Based on these curves, we modified the thickness of the three finest grids in the latest configuration (36, 52 and 76 μm) from 2 mm to 1, 1.4 and 1.7 mm, respectively. Such adjustment improves the modulation efficiency at low energies, without significantly affecting that at high energies. This improvement alone will reduce the cost of grids by at least 10 million RMB and significantly shorten the manufacturing time.

5 DEFINITION AND PROCESSING OF SCIENCE DATA PRODUCTS

The HXI science data products include:

(1) Level 0 data: raw data received from the Mission Operation Center (MOC).
(2) Level 0.5 data: ADC spectral data from all detectors. These data will be released on demand.
(3) Level 1 data: Energy calibrated count spectral data from all detectors. These are the main data product that will be released to the public. Since the energy calibration method may be updated in the future, these data contain information on the calibration version.
(4) Level 1.5 data: Semi-calibrated photon spectral data using only the diagonal elements of the response matrix. These data are applied for imaging and are produced by HXI analysis software at the user's end.
(5) Level 2 data: Reconstructed X-ray images and spectral fitting results. These are also produced by HXI analysis software and OSPEX at the user's end.
(6) Level Q0: Quicklook data based on Level 0 raw data. They will only be used for space weather monitoring and will not be released to the scientific community.
(7) Level Q: Quicklook data based on Level 0.5 data. They include light curves and quicklook spectra.
(8) Level E: Quicklook data for HXI events. They provide light curves, quicklook images and quicklook spectra, which are more detailed compared with Level Q data.

All the data products will be provided in FITS format. IDL SAV files will be provided additionally for Quicklook data.

6 IN-ORBIT SELF-CALIBRATION OF HXI GRIDS

The analysis of calibration spectral data will be performed on the ground, using the spectral line emissions from small radioactive sources implanted in each detector.

The grid parameters will be measured before the launch of ASO-S. However, the vibrations and temperature change during launch may change the alignment of front and rear grids. Therefore, self-calibration must be performed during the test phase of the instrument.

We propose two different methods for self-calibration. The first one is very similar to the method applied for Yohkoh (Sato et al. 1999), which utilizes a large sample of flare data and iterations of imaging. The second one is based on point X-ray sources observed by HXI, produced by extreme compact flares. Such events are rare but very efficient in determining the grid parameters.

For a point source, the collected counts from a single detector behind single subcollimators are determined by the phase of the source in this subcollimator (see Fig. 8(a)). If the front and rear grids are shifted, the phase of the source changes, and so does the count flux. Therefore, we can obtain the changes of phase simply from the ratio of the observed count flux and total flux (from total flux monitor), and then convert it to the relative shift of front and rear grids. Besides, the solar aspect system which consists of two components also monitors the relative changes between the front and rear panels in real time.

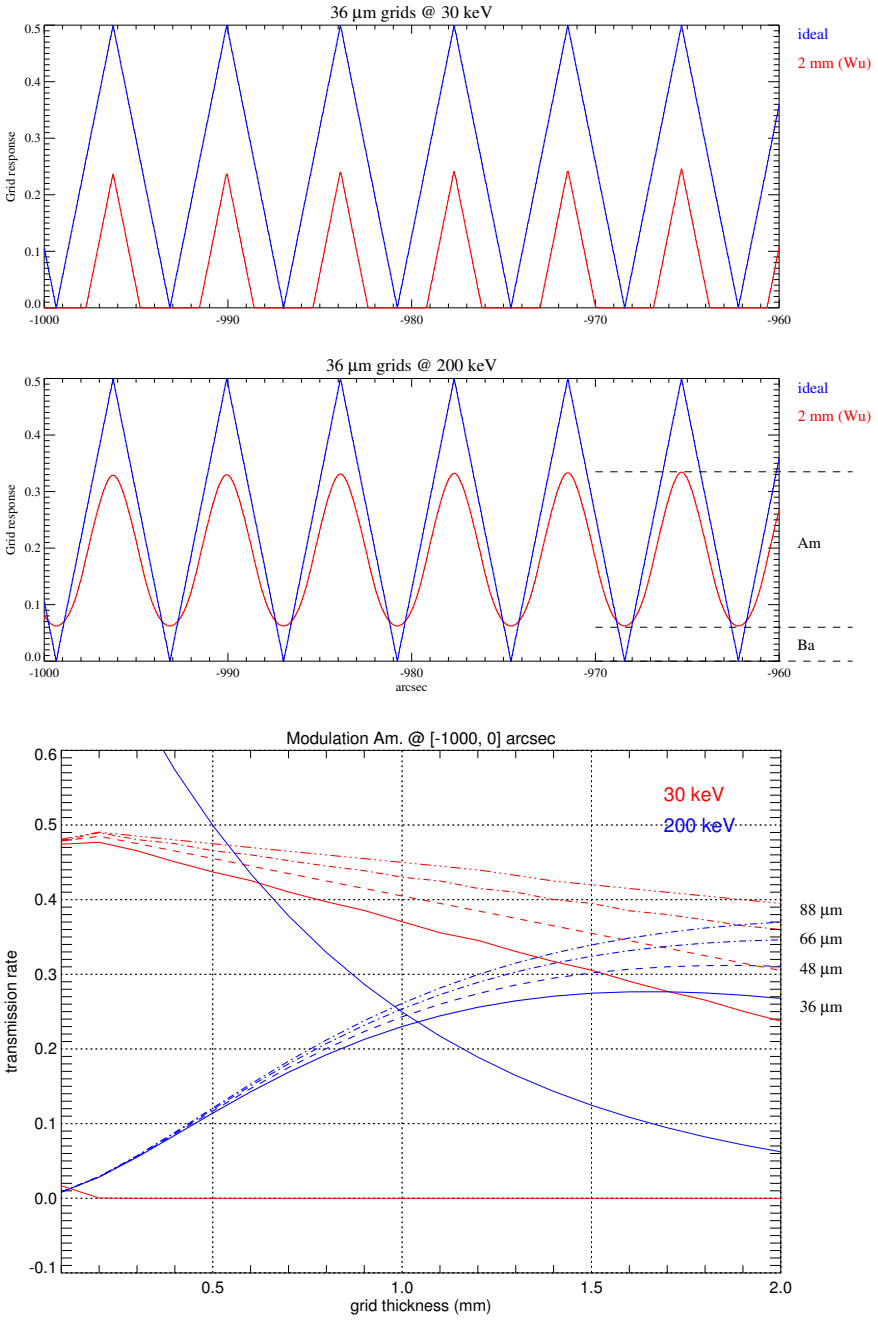

Fig. 7 *Upper*: Ideal (*blue*) and non-ideal (*red*) triangular response functions close to the edge of the normal FOV for 30 keV and 200 keV, respectively. It shows the reduction of modulation amplitude due to the internal shadowing of grids that have a thickness of 2 mm. *Bottom*: Modulation amplitudes at 30 keV and 200 keV as functions of grid thickness for pitch=36, 48, 66, 88 μm. The two thin curves indicate the minimum level of the transmission rate at 30 and 200 keV, respectively, which is zero in the ideal case.

In Figure 8, we show an example of determining relative shifts in a simulated case. The five subcollimators used here have a pitch of 584 μm but different position angles. First, we consider the ideal case. The ideal pattern image at the center of the FOV of one of the subcollimators is displayed in Figure 8(a). Then we consider a point source whose location (In the real case, the source location can be obtained from the imaging result using all subcollimators except the one under calibration.) and phase are indicated by the white cross and black line, respectively. Its phase is also pointed out by the black arrow in the flux-phase plot of Figure 8(b). The expected count fluxes (in units of total flux) from the five subcollimators are plotted against their phases (red symbols) in Figure 8(b). As expected, they are all located along the unified triangular response function. Next, we simulated the real case by randomly shifting the

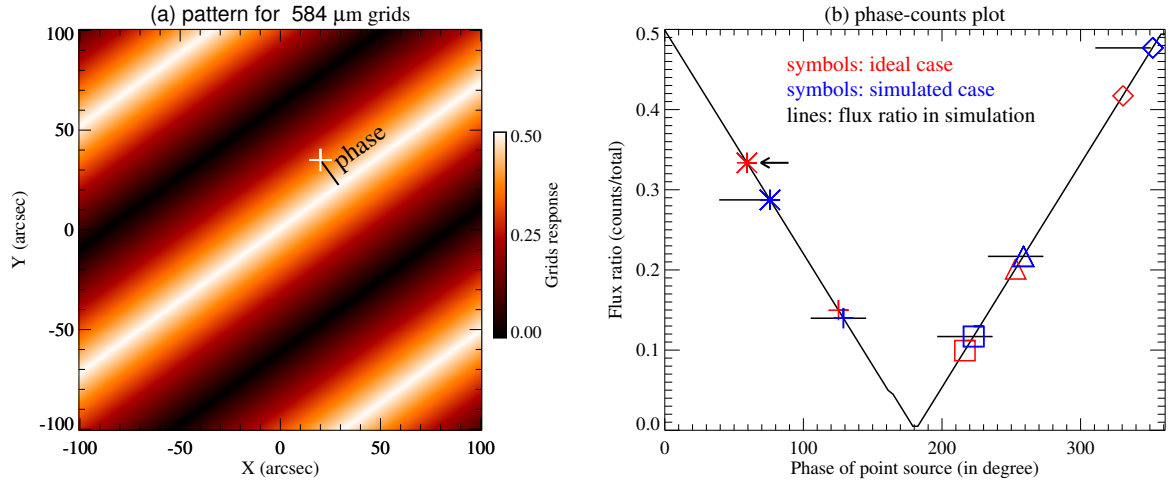

Fig. 8 Explanation of self-calibration method for determining the phase change relative to the ideal case. Panel (a) displays the pattern for a subcollimator with grid pitch = 584 μm. The *white cross* marks the location of the point source used in the calculation. Its phase is indicated by a *black line* and also marked in panel (b) by an *arrow*. Panel (b) depicts the unified triangular response function (response-phase) and the phase-counts plot for the five subcollimators that have the same grid pitch but different position angles. The *red symbols* indicate the phases of the point source in the five subcollimators for the ideal case, and the *blue ones* for the simulated case, where they result from the assumed random shifts between the front and rear grids. The fluxes (in units of total flux) calculated from the simulated case are indicated by the *black lines*. As expected, they cross the triangular response function at the points that have the exact phases in the simulated case.

front and rear grids (in their own planes). It is equivalent to changing the pointing of the grids or the location of the source for each subcollimator. This results in shifting of pattern images and therefore changes in the source phase (note only shifts that are perpendicular to grids cause changes in phase). Since these shifts are known, the corrected pattern images can be obtained. Then we calculated the fluxes (as simulated data) received from each detector behind each subcollimator from the new pattern and new phases (they are marked by the blue symbols in Fig. 8(b).). Finally, in order to identify how much the grids are shifted, we need to first determine the new phases from data. We represent the fluxes from the simulated data (these are what we will get from observations) by the black lines in Figure 8(b). Where they cross the triangular response function should be at the new phases. It is clearly seen that these points of intersection are indeed in good agreement with the blue symbols. This is because (as mentioned above) a point source has only a single response in each subcollimator. Once we obtain the new phases, they can be utilized in corrections to HXI imaging. More details on HXI self-calibration methods will be given in a separate paper.

7 SUMMARY

Like any high energy solar mission, HXI simulation is an important task for the design of HXI grids, the reconstruction of images and the analysis of science data. The HXI science team has developed basic imaging algorithms and performed the simulation work for HXI imaging, grid response, the effect of grid thickness, detector response, background estimation, grid parameters and self-calibration of subcollimators. Some other parameters (such as position angles) are still under study.

In the next phases till the launch of ASO-S, the focus of the HXI science team will shift to the following tasks: (1) the full simulation of a solar flare; (2) more accurate estimation of in-orbit background; (3) the development of HXI software, including codes for imaging algorithms, data processing software, data production software, quick-look software, HXI main frame, imaging software, spectroscopy software and STIX-HXI joint analysis software; (4) development of more imaging algorithms, including a new method based on machine learning.

Acknowledgements This work is supported by the Strategic Priority Research Program on Space Science, Chinese Academy of Sciences (Grant Nos. XDA15320104, XDA15052200 and XDA15320300) and by the National Natural Science Foundation of China (Grant Nos. 11427803, 11820101002, U1731241 and U1631242). Y.S. also acknowledges the 'Thousand Young Talents Plan', and the Jiangsu Innovative and Entrepreneurial Talents Program.

References

Allison, J., Amako, K., Apostolakis, J., et al. 2006, IEEE

Transactions on Nuclear Science, 53, 270
Aschwanden, M. J., Fletcher, L., Sakao, T., Kosugi, T., & Hudson, H. 1999, ApJ, 517, 977
Benz, A. O. 2017, Living Reviews in Solar Physics, 14, 2
Brown, J. C. 1972, Sol. Phys., 26, 441
Casadei, D., Jeffrey, N. L. S., & Kontar, E. P. 2017, A&A, 606, A2
Dennis, B. R., & Pernak, R. L. 2009, ApJ, 698, 2131
Durouchoux, P., Hudson, H., Matteson, J., et al. 1983, A&A, 120, 150
Fletcher, L., Dennis, B. R., Hudson, H. S., et al. 2011, Space Sci. Rev., 159, 19
Gan, W. Q., Zhu, C., Deng, Y. Y., et al. 2019, RAA (Research in Astronomy and Astrophysics), 19, 156
Holman, G. D., Aschwanden, M. J., Aurass, H., et al. 2011, Space Sci. Rev., 159, 107
Hurford, G. J., Schmahl, E. J., Schwartz, R. A., et al. 2002, Sol. Phys., 210, 61
Kilner, J. R., & Nakano, G. H. 1989, in Proc. SPIE, 1159, EUV, X-Ray, and Gamma-Ray Instrumentation for Astronomy and Atomic Physics, eds. C. J. Hailey, & O. H. W. Siegmund, 27
Kosugi, T., Makishima, K., Murakami, T., et al. 1991, Sol. Phys., 136, 17
Krucker, S., Hurford, G. J., Su, Y., & Gan, W. Q. 2019, RAA (Research in Astronomy and Astrophysics), 19, 167
Lin, R. P., Dennis, B. R., Hurford, G. J., et al. 2002, Sol. Phys., 210, 3
Mertz, L. N., Nakano, G. H., & Kilner, J. R. 1986, Journal of the Optical Society of America A, 3, 2167
Priest, E. R., & Forbes, T. G. 2002, A&A Rev., 10, 313
Raymond, J. C., Krucker, S., Lin, R. P., & Petrosian, V. 2012, Space Sci. Rev., 173, 197
Sato, J., Kosugi, T., & Makishima, K. 1999, PASJ, 51, 127
Shibata, K., & Magara, T. 2011, Living Reviews in Solar Physics, 8, 6
Warmuth, A., & Mann, G. 2013, A&A, 552, A86
Zhang, Z., Chen, D. Y., Wu, J., et al. 2019, RAA (Research in Astronomy and Astrophysics), 19, 160